# Soft landing stability analysis of a Mars lander under uncertain terrain

Yang DONG [a], Jianzhong DING [a],\*, Chunjie WANG [b], Hui WANG [a], Xueao LIU [a]

[a] *School of Mechanical Engineering and Automation, Beihang University, Beijing 100191, China*
[b] *State Key Laboratory of Virtual Reality Technology and Systems, Beihang University, Beijing 100191, China*

**Abstract**    Safe soft landing of the lander is vital to the Mars surface exploration mission. Analysis and verification of the landing stability under uncertain terrain play an important role in lander design. However, the effect of uncertain terrain is ignored in most existing studies, making the analysis incomprehensive and increasing the risk of landing failure in practice. In this paper, a Mars lander with 10 attitude control thrusters is introduced and its dynamics model is then established considering plastic deformation parts and nonlinear contact forces. The effectiveness and accuracy of the dynamics modeling method are verified by experiments with an average relative error of 10%. In order to carry out the dynamics simulation with high-fidelity terrain, a terrain generation method based on statistical data is proposed. Through Monte Carlo simulation under a 50 m × 50 m randomly generated landing terrain, the stability of the lander and the effects of attitude control thrusters are analyzed. The results show that the failure rate is 5.5%, in which the primary failure forms are overturning and abnormal attitude. When the landing simulations are repeated without thrusters, the stable ratio decreases from 94.5% to 90.7%, suggesting the positive effects of attitude control thrusters in improving landing stability under rough terrain.

## 1. Introduction

With the development of deep space technology, one detector after another was launched to extraterrestrial planets, satellites, and small celestial bodies. Soft landing on celestial bodies is important and challenging in deep space exploration missions, especially in missions that need to land rovers safely on celestial bodies with high gravity, such as the Moon and Mars[1–4]. Recently, the successful landing of Perseverance[5] and the launch of the Chinese first Mars lander Tianwen-1[6] have attracted extensive attention of researchers and made Mars exploration a research hotspot. Ways to alleviate the vibration and reduce the impact effectively during the landing process are key concerns in designing a lander. Among all the landing schemes, landing with legged landing gear is well-appraised and widely used due to its simple structure and high reliability[7–10].

In order to design a high-stability soft landing lander, it is necessary to fully evaluate and optimize its soft landing performance before launching it onto the outer space planet[11–12]. Physical experiments and dynamics simulations are currently the two most effective means of analyzing the soft landing performance. Although experiments with prototypes have high credibility[13–14], the difficulty in non-earth gravity simulation and high prototype manufacturing cost make the experiments only capable of evaluating limited landing cases. On the contrary, the dynamics simulation is cheap, and it has the advantage of simulating complex landing conditions. Therefore, the finite element (FE) method[15] and the multi-rigid-body method are widely used for soft landing simulations. The FE method is suitable for analyzing highly nonlinear systems, including large deformation, nonlinear material, and contact[16]. Some researchers established the FE model of landers to analyze the structural response under harsh loading conditions[17]. The multi-rigid-body dynamics modeling and analysis method assume that the components are rigid and focus on the macro information such as velocity and displacement during landing. Although the information of deformation and stress is ignored, this method has the advantages of fast computation and low computer memory consumption, which make it widely used in configuration optimization, limit condition traversal, stability boundary analysis, and Monte Carlo simulation[18–19]. However, errors that arisen from simplification should be considered to give a reliable prediction.

In the process of lander modeling, two issues require special attention. One issue is the simulation of contact forces between the footpads and landing terrain, which may significantly affect simulation accuracy. Nonlinear spring damping model[20], plastic contact model[21], and model based on force–displacement curve[22] were developed for contact modeling in recent studies. The other issue is the modeling of landing terrain. Generally, researchers simulated the soft landing using an ideal flat plane to simulate the landing terrain. However, the assumption of landing on an ideal flat plane neglecting the influence of rocks and meteorite craters leads to deviations in the results between simulation and landing in practice. Establishing complex landing terrain based on measured data is helpful for comprehensive analysis of landing performance, such as the studies of Rosetta Lander (comet exploration)[23–24]. However, it is impossible to analyze the landing terrain completely. For landing on Mars, landing stability in rugged terrain can only be guaranteed by landing gear design and automatic control of attitude thrusters. Therefore, the stability of Mars lander under uncertain terrain needs to be studied deeply.

The Mars lander considered in this paper uses the shutdown-at-touchdown[25–26] landing mode to reduce the landing velocity and impact force. In addition, 10 attitude control thrusters belonging to Guidance Navigation Control (GNC) system are considered. We aim to activate them during landing to improve the terrain adaptability stability. The main contribution of this paper is that an advanced terrain simulation method is proposed for landing performance evaluation. A high-fidelity dynamics model of the legged Mars lander is established, and its accuracy is verified by prototype experiments. Using the proposed terrain generation methods, the effects of uncertainties of the landing terrain are investigated for the first time, which helps estimate the landing performance comprehensively. It enriched the study on Mars landing and

the results provide theoretical support for the Chinese Mars exploration project. Moreover, the effectiveness of attitude control by thrusters is verified.

The rest of the paper is organized as follows. Section 2 presents the lander configuration and the arrangement of attitude control thrusters. In Section 3, the dynamics model is derived considering plastic deformation parts and nonlinear contact forces. Section 4 introduces the terrain generation method, and the dynamics model is verified by experiments in Section 5. In Section 6, Monte Carlo simulation in uncertain terrain is carried out and the effectiveness of the attitude control strategy is further analyzed. Finally, conclusions are drawn in Section 7.

## 2. Lander configuration

The Mars lander discussed in this paper is equipped with four sets of inverted-triangle landing gears, which are centrosymmetric and distributed around the main body. Each landing gear is mainly composed of a buffer rod, a primary strut, two secondary struts, and a footpad, as shown in Fig. 1. The top end of the buffer rod is fixed on the main body, and the other end is connected with the primary strut through a universal joint. One part of the secondary strut (outer cylinder) is connected with the main body by a universal joint, and the other part (inner cylinder) is connected with the footpad through a ball hinge. Due to the large cushioning capacity of the secondary strut, the primary strut does not provide cushioning and is fixed with the footpad.

As shown in Fig. 2, a main engine is installed at the bottom of the lander for braking. When the footpad first contacts the Martian surface, the main engine begins to shut down. This landing strategy is called shutdown-at-touchdown mode. A certain amount of time is required for signal acquisition, decision, and shutdown operations after being touched down, which delays the shutdown process. In this case, the thrust of the main engine adversely affects the landing stability[27]. An attitude control system is applied to the lander to improve the landing adaptability and stability. 10 thrusters are installed to control the attitude during landing, two of which are fixed on the upper plane of the main body, labeled as $A_1$ and $A_2$, respectively. And the rest of the thrusters are equipped on the bottom of the main body, labeled from $B_1$ to $B_8$. O-XYZ is the ground coordinate system whose $OX$ axis points



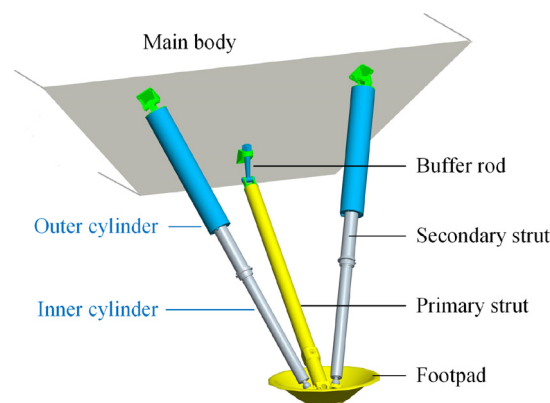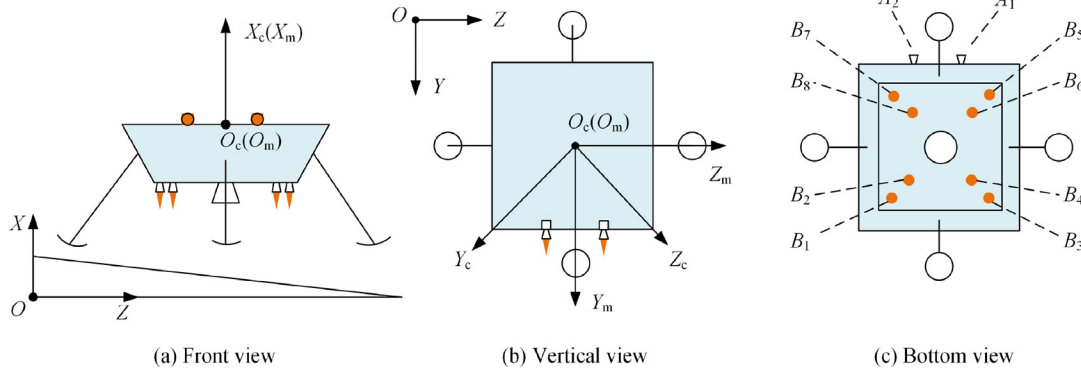**Fig. 1**    Landing gear configuration.

**Fig. 2**　Coordinate systems and thrusters' position.

upwards against the gravitational direction, and the $OZ$ axis points northwards of Mars. $O_m$-$X_mY_mZ_m$ is a body coordinate system fixed on the main body, whose $O_mX_m$ axis is the symmetry axis of the lander, and the $O_mY_m$ axis is parallel to the nozzle of $A_1$. $O_c$-$X_cY_cZ_c$ is a control coordinate system whose $O_c$ and $O_cX_c$ axis coincide with the body coordinate system. The angle between the $O_cZ_c$ and the $O_mZ_m$ is 45 °.

## 3. Dynamics modeling

### 3.1. Landing conditions

From a macro point of view, landing is a collision process between two objects. The landing conditions include relative velocity, relative angular velocity, and relative attitude. In order not to lose generality, landing conditions are divides into three groups.

(1) Slope parameters $\{\alpha_s, \beta_s\}$.

Considering that Mars has a gravity of about 3.72 m/s², the gravity effect is more evident than landing on the Moon (about 1.63 m/s²) or a small celestial body (almost no gravity). Therefore, the overall slope of the landing surface has a significant effect on the landing stability, and especially, it increases the risk of overturning. Here, the slope of the datum plane of the landing terrain $\alpha_s$ and the orientation of the slope in $O$-$XYZ$ $\beta_s$ (as shown in Fig. 3) are considered. Since the surface of any celestial body is not entirely flat, these two parameters
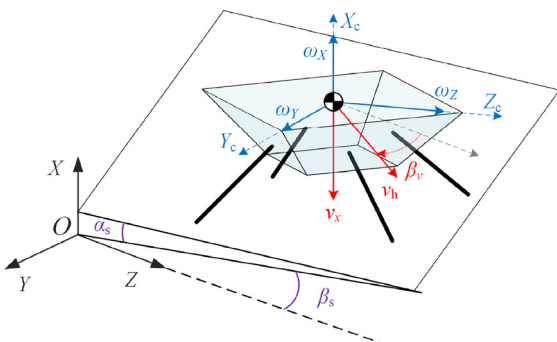
are only the overall slope of the landing area. In the dynamics model, rocks and craters are included.

(2) Velocities $\{v_h, \beta_v, v_x\}$.

Before contact, all parts of the lander have the same velocity relative to $O$-$XYZ$. Here, the horizontal velocity $v_h$, the direction $\beta_v$, and the vertical velocity $v_x$ are considered.

(3) Lander attitude $\{\theta_Z, \theta_X, \theta_Y\}$ and angular velocities $\{\omega_X, \omega_Y, \omega_Z\}$.

Rotate $O$-$XYZ$ to make it parallel to $O_c$-$X_cY_cZ_c$ by $Z$-$X$-$Y$ rotation sequence and denote the rotation angles as $\theta_Z, \theta_X, \theta_Y$, respectively. The angular velocity vectors projected on $X_c$, $Y_c$, $Z_c$ are denoted as $\omega_X$, $\omega_Y$, $\omega_Z$, respectively. These attitude parameters are also the input of subsequent attitude control.

### 3.2. Nonlinear buffering force

The cushion material that connects the inner and outer cylinder of the secondary struts is the main energy-absorbing component through unidirectional plastic deformation. Its mechanical properties have been reported in detail in the literature[17]. Since we focus on the macroscopic dynamic characteristics of the lander, the detailed parameters and characteristics of this material are not repeatedly discussed here. The nonlinear relationship between the axial buffering force and the buffering stroke obtained in practice is shown in Fig. 4. Discretely measured points are interpolated by Cubic Spline Inter-
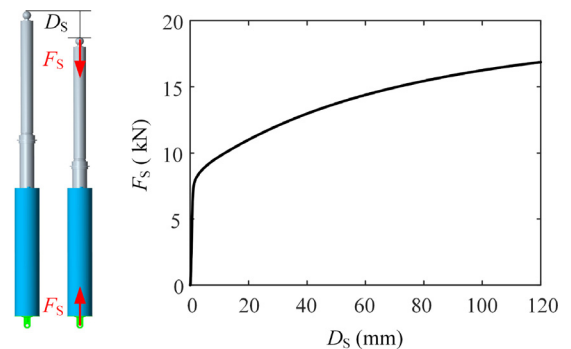


**Fig. 3**　Landing conditions.



**Fig. 4**　Secondary strut buffering force.

polation to simulate the force in the multi-body dynamics model. It should be noted that the buffering force is only capable when compression and the expression of the buffering force is

$$
F_S(D_S, \dot{D}_S) = \begin{cases} \sum_{i=0}^{n} f_i(D_S) & \dot{D}_S \geqslant 0 \\ 0 & \dot{D}_S < 0 \end{cases} \tag{1}
$$

where $F_S$ is the axial buffering force, $D_S$ is the buffering stroke, $f_i$ is the piecewise cubic polynomial.

### 3.3. Pseudo-rigid-body model of buffer rod

The buffer rod is used to absorb the impact between the primary strut and the main body. Plastic deformation occurs when the buffer rod is subjected to impact, and its deformation form is mainly bending. In order to simplify the dynamics model, the buffer rod is equivalently substituted with a pseudo-rigid-body model[25,28–29], as shown in Fig. 5. The buffer rod is modeled with two rigid links, a revolute joint, and a prismatic joint. Angle $\alpha_E$ is used as the independent variable. The changes of moment $M_E$ and axial displacement $S_E$ with respect to angle $\alpha_E$ are obtained by experiment, as shown in Fig. 6. Analogously, discretely measured points are interpolated by Cubic Spline Interpolation.

### 3.4. Contact force

The contact force between the footpad and the landing terrain contains two parts, namely, the normal force and the tangential force. We adopt the nonlinear spring-damping model[20] to simulate the normal force, which can simulate the fact that the stiffness increases when the penetration depth increases. For the tangential force, some studies used the Coulomb friction for simulation. However, in the actual landing process, as shown in Fig. 7, the footpad may get trapped in the soil. In this situation, in addition to the friction proportional to the positive pressure, there will be additional damping relate to tangential velocity. The coefficient of this damping will also increase with the penetration depth.

Since the traditional Coulomb friction model is no longer effective in accurately simulating the tangential mechanical characteristics, we modified the classic expression by adding a new depth-dependent damping term in the tangential force model as
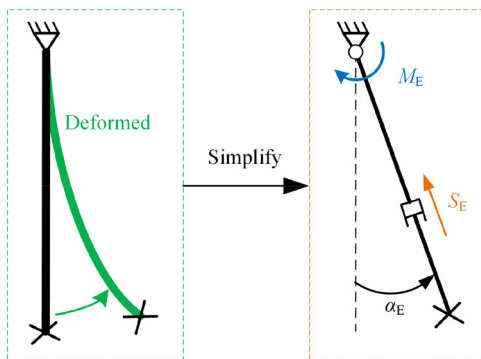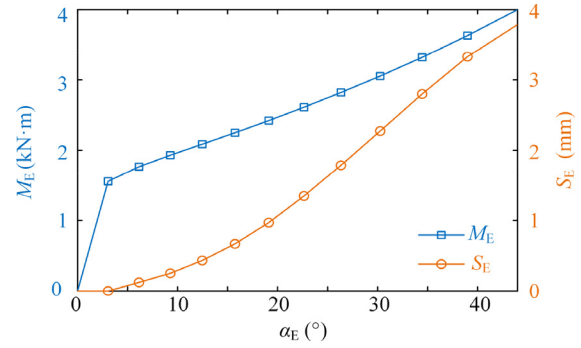


**Fig. 5**    Pseudo-rigid-body model.
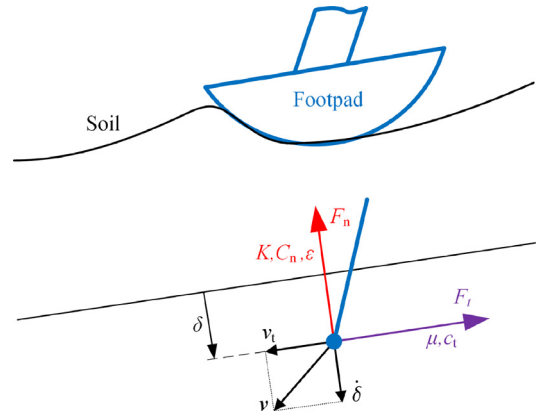


**Fig. 6**    Mechanical behavior of buffer rob.



**Fig. 7**    Contact model.

$$
\begin{cases} F_n = K\delta^\varepsilon + C_n\dot{\delta} \\ F_t = \mu F_n + C_t v_t \\ C_t = c_t \delta \end{cases} \tag{2}
$$

where $F_n$ is the normal force that perpendicular to the landing terrain, $K$ is stiffness coefficient, $\delta$ is the normal penetration depth, $\varepsilon$ is exponent parameter, $F_t$ is the tangential force that is opposite to the tangential velocity $v_t$, $\mu$ is friction coefficient, $C_n$ and $c_t$ are damping coefficients. The values of these parameters are shown in Table 1.

### 3.5. Thrust modeling

The attitude control thrusters are used to reduce the risk of overturning, which work for two seconds when the main engine has shut down. The control strategy concerns the instant attitude and angular velocity of the lander. When they

**Table 1**    Parameters of contact model.

| Parameters | Values |
|---|---|
| $K$ (Nm$^{-\varepsilon}$) | $4.88 \times 10^7$ |
| $\varepsilon$ | 3.43 |
| $\mu$ | 0.41 |
| $C_n$ (Ns/m) | $3.6 \times 10^5$ |
| $c_t$ (Ns/m$^2$) | $4.72 \times 10^6$ |

deviate from the ideal situation ($\theta_i = \omega_i = 0$, $i = X, Y, Z$), the control torques are computed as

$$\begin{cases} T_X = a\theta_X + k_1\omega_X \\ T_Y = b\theta_Y + k_2\omega_Y \\ T_Z = b\theta_Z + k_2\omega_Z \end{cases} \quad (3)$$

where $a$ and $b$ are control coefficients, $k_i$ is the angular velocity damping coefficient.

In practice, there are two situations to be considered. That is, there is a maximum thrust limitation for each thruster, and thrusters can only provide unidirectional force. Therefore, the thrust of a specific thruster is calculated according to the torque symbol and force arm, as

$$\begin{cases} F_{A1} = \min\{|T_X|/L_1, \; F_{M1}\} \; T_X < 0 \\ F_{A2} = \min\{|T_X|/L_1, \; F_{M1}\} \; T_X \geqslant 0 \\ F_{B1} = F_{B2} = \min\{|T_Y|/2L_2, F_{M2}\} \; T_Y \geqslant 0 \\ F_{B5} = F_{B6} = \min\{|T_Y|/2L_2, F_{M2}\} \; T_Y < 0 \\ F_{B3} = F_{B4} = \min\{|T_Z|/2L_2, F_{M2}\} \; T_Z < 0 \\ F_{B7} = F_{B8} = \min\{|T_Z|/2L_2, F_{M2}\} \; T_Z \geqslant 0 \end{cases} \quad (4)$$

where $F_{A1}$, $F_{A2}$, $F_{Bi}$ are the thrusts of $A_1$, $A_2$, and $B_i$ thrusters, respectively, $F_{M1}$ and $F_{M2}$ are the maximum allowable thrusts of $A$ and $B$ series control thrusters, and $L_1$ and $L_2$ are force arms. All control parameters are presented in Table 2.

### 3.6. Dynamics model

In this paper, the Lagrange dynamic equations are used to deduce the dynamics model of the Mars lander. An overview of the three-dimensional lander simulation model is shown in Fig. 8. After simplification, the whole model contains 29 rigid parts and 40 groups of constraints, including 12 translational joints, 12 universal joints, 8 spherical joints, 4 revolute joints, and 4 $\alpha_E$ -$S_E$ constraints. Some necessary parameters of the lander are presented in Table 3.

The centroid position and Euler angle of each rigid part with respect to $O\text{-}XYZ$ are considered generalized coordinates, and the dynamics equations are expressed as
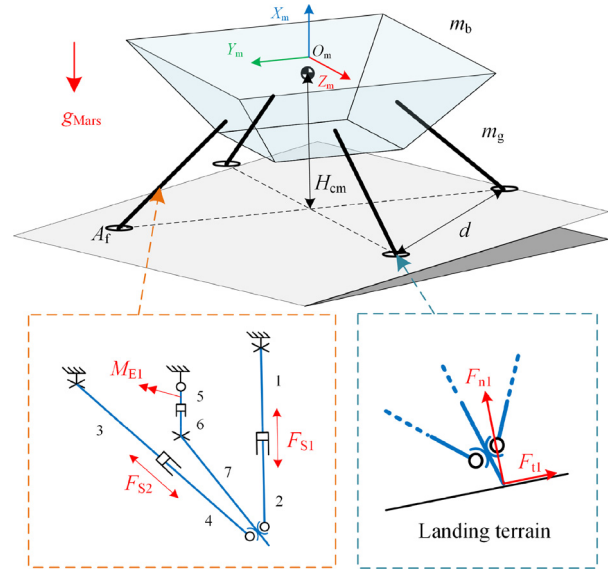
$$\begin{bmatrix} M & C_q^T \\ C_q & 0 \end{bmatrix} \begin{bmatrix} \ddot{q} \\ \lambda \end{bmatrix} = \begin{bmatrix} Q_e + Q_v \\ Q_d \end{bmatrix} \quad (5)$$

where

$$Q_d = -C_{tt} - (C_q\dot{q})_q\dot{q} - 2C_{qt}\dot{q} \quad (6)$$



**Fig. 8** Overview of three-dimensional lander simulation model.

**Table 3** Parameters of the Mars lander.

| Parameters | Values |
|---|---|
| Mass of main body $m_b$ (kg) | 876 |
| Mass of each landing gear $m_g$ (kg) | 10.5 |
| Distance between two adjacent footpads $d$ (m) | 2.23 |
| Height of center of mass $H_{cm}$ (m) | 0.879 |
| Maximum contact area of footpad $A_f$ (m$^2$) | 0.0314 |

where $M$ is the mass matrix, $C$ is $156 \times 1$ constraint function vector, $q$ is $174 \times 1$ generalized coordinates vector, $C_q$ is the first partial differentiation of $C$ with respect to $q$, $\lambda$ is the vector of Lagrange multipliers, $Q_v$ is the vector of generalized inertial forces, the subscript $t$ denotes partial differentiation with respect to time, and $Q_e$ is generalized external force vector, as

$$Q_e = G + F_S + M_E + F_C + F_T \quad (7)$$

where $G$ is gravity, $F_S$ is buffering forces of the secondary strut, $M_E$ is the equivalent moments of buffer rods, $F_C$ is contact forces, and $F_T$ is thrust.

The Runge-Kutta method is used to solve the dynamic differential equations. The integral step is 0.001 s with a total simulation time of 10 seconds.

## 4. Uncertain landing terrain modeling

In order to comprehensively evaluate the landing performance of the lander landing in irregular terrain, we aim to obtain a local terrain model which can be used in dynamics simulation. It is rather difficult to express the terrain surface with an analytical formula. However, according to the existing techniques, the terrain can be modeled with two common characteristics: meteor craters and rocks. Since the comprehensive terrain data of Mars is not available, the terrain model is established, referring to the statistical data of the distribution of lunar rocks and craters. According to the literature[30], typical distributions of

**Table 2** Parameters of control coefficients.

| Parameters | Values |
|---|---|
| $a$ (N/(°)) | 17.45 |
| $b$ (N/(°)) | 12.21 |
| $k_1$ (Ns/(°)) | 26.18 |
| $k_2$ (Ns/(°)) | 17.45 |
| $F_{M1}$ (N) | 20 |
| $F_{M2}$ (N) | 200 |
| $L_1$ (m) | 1.21 |
| $L_2$ (m) | 1.15 |

craters and rocks on the lunar surface can be approximately expressed as

$$N_c(D_c) = 10^{-1}D_c^{-2} \quad D_c \in [0.2, 40] \text{ m} \tag{8}$$

$$N_b(D_b) = \begin{cases} 10^{-2.52}D_b^{-2.15} & D_b \in [0.05, 0.76] \text{ m} \\ 10^{-2.62}D_b^{-3.01} & D_b \in [0.76, 2.00] \text{ m} \end{cases} \tag{9}$$

where $D_c$ is the diameter of a crater, $D_b$ is the diameter of a rock, $N_c$ is the accumulated number of craters larger than $D_c$ per 1 m$^2$, $N_b$ is the accumulated number of rocks larger than $D_b$ per 1 m$^2$. Craters with $D_c < 0.2$ m and rocks with $D_b < 0.05$ m are removed because tiny craters and rocks have little effect on the process of landing.

The shape of a crater is usually irregular, which brings great difficulties in modeling. In this paper, we assume that craters are all in the regular shape expressed as

$$z_c(x, y) = \frac{-D_c^2}{12\pi r(x, y)}\sin\frac{2\pi r(x, y)}{D_c} \quad r < D_c \tag{10}$$

where

$$r(x, y) = \sqrt{(x - x_0)^2 + (y - y_0)^2} \tag{11}$$

where $(x_0, y_0)$ is the center of the crater. Analogously, the expression of the shape of a rack is

$$z_b(x, y) = \frac{-2r(x, y)^2}{D_b} + \frac{D_b}{2} \quad r < \frac{D_b}{2} \tag{12}$$

Examples of a crater and rock are shown in Fig. 9.



(a) $D_c$=1 and $(x_0, y_0)$=(0,0)
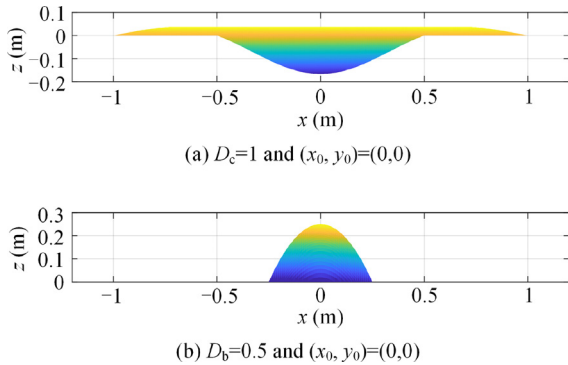


(b) $D_b$=0.5 and $(x_0, y_0)$=(0,0)
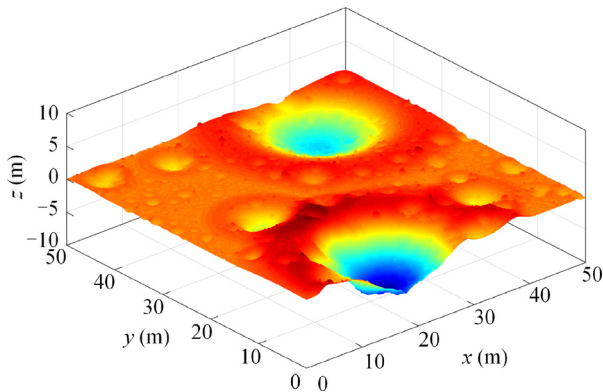
**Fig. 9**    Examples of crater and rock.



**Fig. 10**    Generated landing terrain.

Now that we have the expressions in Eqs. (8)-(12), craters and rocks are randomly generated on a 50 m × 50 m landing plane using the proposed Algorithm 1 in the following. And the generated terrain is shown in Fig. 10.

| **Algorithm 1** Randomly terrain generation |
|---|
| 1: Inputs: Given terrain length $l_1$ and width $l_2$ |
| 2: **Step1**: Compute the set of craters diameters $I_c$ |
| 3: $I_c = \varnothing$ |
| 4: Terrain area $S = l_1 l_2$ |
| 5: Solve equation: $N_c(D_c) S = 1$, obtain $D_{cmax}$ |
| 6: **while** $D_{cmax} > 0.2$ |
| 7: Generate random number $p \in [0,1]$ |
| 8: $D_{now} = pD_{cmax}$ |
| 9: $I_{used} = \{D_c \mid D_c \in I_c, D_c > D_{now}\}$ |
| 10: $N_{used} = $ card $(I_{used})$ |
| // card($\bullet$) return the number of elements in a set |
| 11: $N_t = N_c(D_{now})$ |
| 12: $N_r = N_t - N_{used}$ |
| 13: **if** $N_r < 0$ |
| 14: $D_{cmax} = D_{now}$ |
| 15: $D_{now} = 0$ |
| 16: **else** |
| 17: $I_c \leftarrow I_c \cup \{D_{now}\}$ |
| 18: **end** |
| 19: **end** |
| 20: **Step2**: Compute the set of rocks diameters $I_b$ |
| 21: ... (*Similar to step1*) |
| 22: **Step3**: Generate random position $x_0 \in [0, l_1]$ and $y_0 \in [0, l_2]$ for all elements of $I_c$ and $I_b$ |
| 23: **Step4**: Calculate the shape for all elements by Eqs. (10)-(12) |
| 24: **Step5**: Superimpose and output terrain |

## 5. Model validation

Model updating technology[31–33] is used to improve the accuracy of the dynamics model. In order to reduce the difficulty of the experiment, the landing terrain is a plane, and the effects of the thrusters are not included in the experiment. Experiment facilities are illustrated in Fig. 11.

The experiment is conducted with the following steps:

(a) Connect the prototype with the double-rocker linkage. Pull it to a certain height and then release the lander.
(b) Unchain the prototype from the double-rocker linkage at the lowest position to give the prototype an initial horizontal velocity.
(c) Prototype lands on the slope.

Landing conditions are simulated by adjusting the attitude control device, the release height of the prototype, and the slope of the landing terrain. A high-speed camera system is
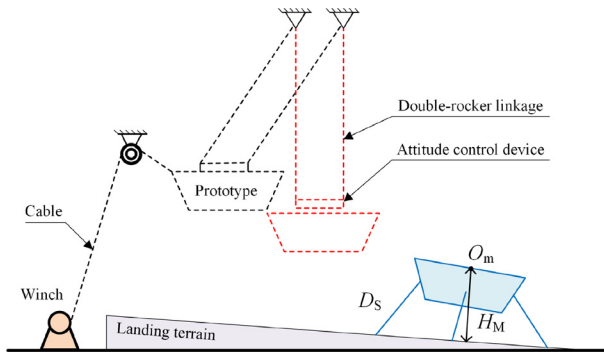
**Fig. 11** Experiment facilities.

used to measure the landing velocity and attitude. Meanwhile, the minimum distance between $O_m$ and the landing terrain ($H_M$ $H_M$) and the secondary struts buffering strokes ($D_S$ $D_S$) are measured. More details are discussed in the literature[34].

**Table 4** Landing parameters of the experiment.

| Parameter | Case 1 | Case 2 |
|---|---|---|
| $\alpha_s$ (°) | 0.00 | 0.00 |
| $\beta_s$ (°) | 0.00 | 8.00 |
| $v_h$ (m/s) | 0.99 | 1.29 |
| $\beta_v$ (°) | 180.00 | 0.00 |
| $v_x$ (m/s) | 2.86 | 3.01 |
| $\theta_Y$ (°) | −0.09 | 0.55 |
| $\theta_X$ (°) | 45.12 | 45.12 |
| $\theta_Z$ (°) | 0.16 | 0.26 |

Two sets of experimental data were used for validation, and landing conditions are presented in Table 4.

In case 1, there is no slope (0°) and the landing speed is relatively low, so the landing performance can be preliminarily tested. Case 2 increases the slope (8°) and the landing speed, which can further test the performance under adverse conditions.

Landing parameters in the simulation are set according to Table 4. The comparison between simulation and experiment is shown in Fig. 12. The simulation results show that the proportion trend of $D_S$ between different legs is close to that of the experiment. The average error of $D_S$ is 2.80 mm, and the average relative error is 10.5%. The average error of $H_M$ is 2.17 mm with a relative error of 0.25%. For the experiments, the measurement accuracy and manufacturing error can affect the results. Therefore, since relative errors are within the acceptable ranges, the accuracy of the dynamics model is verified.

## 6. Stability analysis

### 6.1. Stable criterion

This paper focuses on the stability of soft landing under the shutdown-at-touchdown mode, which mainly considers anti-overturning ability, buffering performance, and the attitude after landing. Observations indicating the landing performance and stability are chosen as follows.

(1) $L_{min}$ ($> 50$ mm). Minimum distance from the center of mass to the overturning plane[12]. The overturning plane is defined as the vertical plane passing through the centers of two adjacent footpads. This variable indicates the ability to resist overturning. When $L_{min}$ is close to zero, the lander has a high risk of overturning.
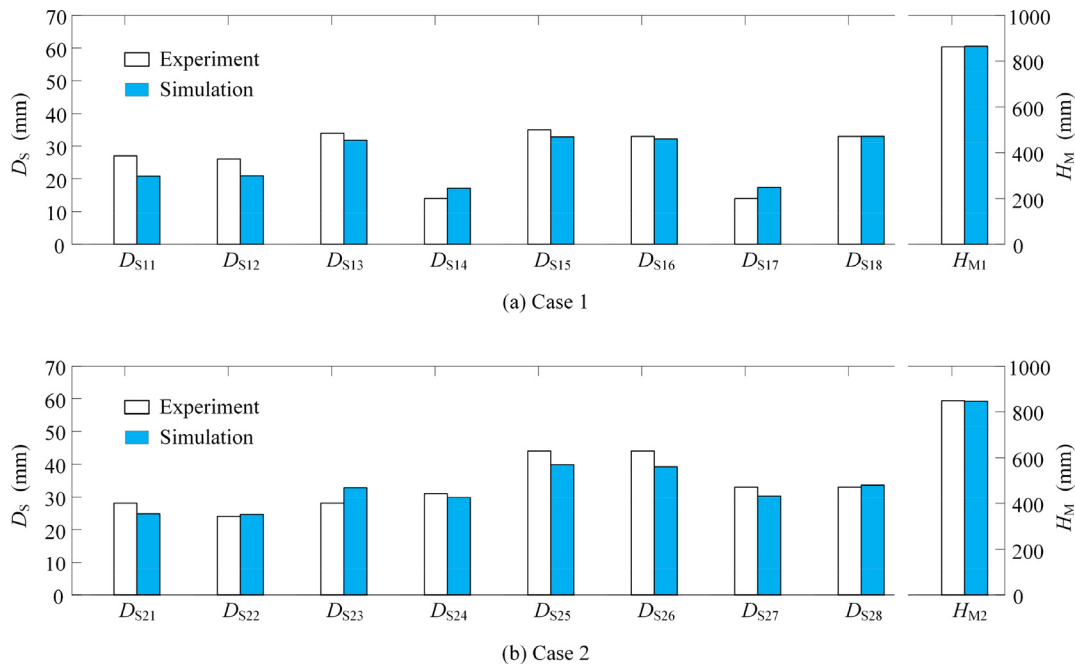


(a) Case 1



(b) Case 2

**Fig. 12** Simulation and experiment results.

(2) $H_{\min}$ ($> 200$ mm). Clearance between the nozzle of the main engine and the landing terrain. If $H_{\min}$ is small, the nozzle may collide with rocks, resulting in damage.

(3) $\alpha_{\mathrm{Emax}}$ ($< 30°$). The maximum rotation angle of buffering rod.

(4) $D_{\mathrm{Smax}}$ ($< 100$ mm). The maximum buffering stroke of secondary struts.

(5) $A_{\max}$ ($< 150$ m/s$^2$). The maximum acceleration of the main body.

(6) $\psi$ ($< 20°$). The angle between the $Y_m$-$Z_m$ plane and the slope after landing. If $\psi$ is large, when the rover departs from the lander, the rover may collapse during the transfer process and result in mission failure.

### 6.2. Monte Carlo simulation

Due to uncertain factors such as external disturbance, landing velocities and attitude cannot be accurately determined. Generally, these parameters are constrained in particular ranges. Therefore, the simulation under certain conditions is not effective to completely evaluate the landing stability, especially when effects of random terrain are considered. Monte Carlo simulation[35] is an alternative to deal with such uncertain problems. This method is based on statistical sampling for numerical calculation, and the more simulation samples are, the more accurate the results are. The computational cost of multi-body dynamics simulation is relatively low and suitable for a large amount of computations.

The Monte Carlo Simulation analysis process is shown in Fig. 13. The first step is to generate the 50 m × 50 m landing terrain using Algorithm 1. Then the next step is to generate the landing conditions and select the landing position randomly on

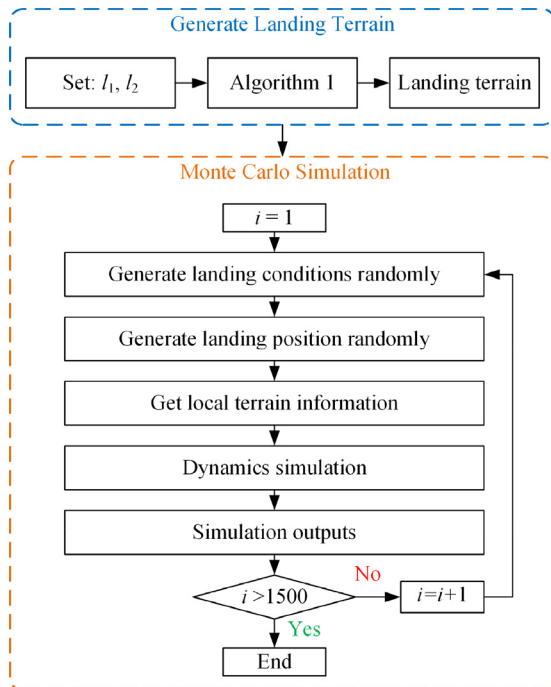the landing terrain with equal probability. According to the actual design capability, the probability distribution of landing attitude and landing velocity are listed in Table 5. Here, $\beta_v$ obeys uniform distributions, and other landing conditions are assumed to obey normal distributions.

It is noteworthy that when the lander lands, each footpad only contacts a small area of the landing terrain. Therefore, it is necessary to obtain local slope, craters, and rocks information according to the landing site before dynamic simulation. The final step is to carry out dynamics simulation and output results. In this paper, a total of 1500 simulation samples are obtained.

The distribution histograms of the Monte Carlo Simulation results are shown in Fig. 14. As shown in Fig. 14(a), in 5.0% of the simulation samples, the lander overturns ($L_{\min} < 50$ mm). Most $H_{\min}$ is distributed in the safe range of [300, 500] mm, as shown in Fig. 14(b), and 0.6% of $H_{\min} < 200$ mm because of rocks. The maximum rotation angle of the buffering rod $\alpha_{\mathrm{Emax}}$, the maximum buffering stroke of the secondary strut $D_{\mathrm{Smax}}$ and the maximum acceleration of main body $A_{\max}$ are all in the safe range and far away from the dangerous threshold, as shown in Fig. 14(c)-(e). In some cases, the angle between the $Y_mO_mZ_m$ plane and the landing terrain $\psi$ exceeds the safe threshold, with a ratio of 0.5% (overturning samples are excluded).

The simulation results suggest that the lander has a stable landing ratio of 94.5% when landing randomly on the generated landing terrain. The overall insecurity rate is 5.5%, and the primary failure forms are overturning and abnormal posture caused by rough topography, while the buffering design is redundant.

Fig. 15(a) shows all the landing sites on the generated terrain and Fig. 15(b) shows regional stability with a 5 m × 5 m division. Overall, most areas have 100% stability and the unstable landing sites can be divided into two types. (1) Landing sites are located at the inner edges of large craters (craters A and C), where a high equivalent slope exists. The regional stability of this part is about 80%. (2) Most of the unstable landing sites are near the area between crater B and C, where the terrain is rugged, and the heights vary dramatically. The regional stability of this area decreased significantly to less than 50%.

### 6.3. Effects of attitude control

In previous analysis results, $L_{\min}$ is the most critical indicator of landing stability. The primary purpose of attitude control is to improve the anti-overturning ability. In order to quantitatively evaluate the effect of attitude control thrust on stability, another 1500 dynamics simulations are performed. The landing parameters of these simulations, including attitude, velocity, and landing sites, are the same as those in Section 6.2 that the only difference is that attitude control thrusters are deactivated.



**Fig. 13** The Monte Carlo Simulation process.

**Table 5** Probability distribution of landing conditions.

| Landing parameter | Distribution |
| --- | --- |
| $v_x$ (m/s) | $N(2, 0.4^2)$ |
| $v_h$ (m/s) | $N(0, 0.3^2)$ |
| $\beta_v$ (°) | $U(0, 360)$ |
| $\theta_X, \theta_Y, \theta_Z$ (°) | $N(0, 1^2)$ |
| $\omega_X, \omega_Y, \omega_Z$ ((°)/s) | $N(0, 1^2)$ |
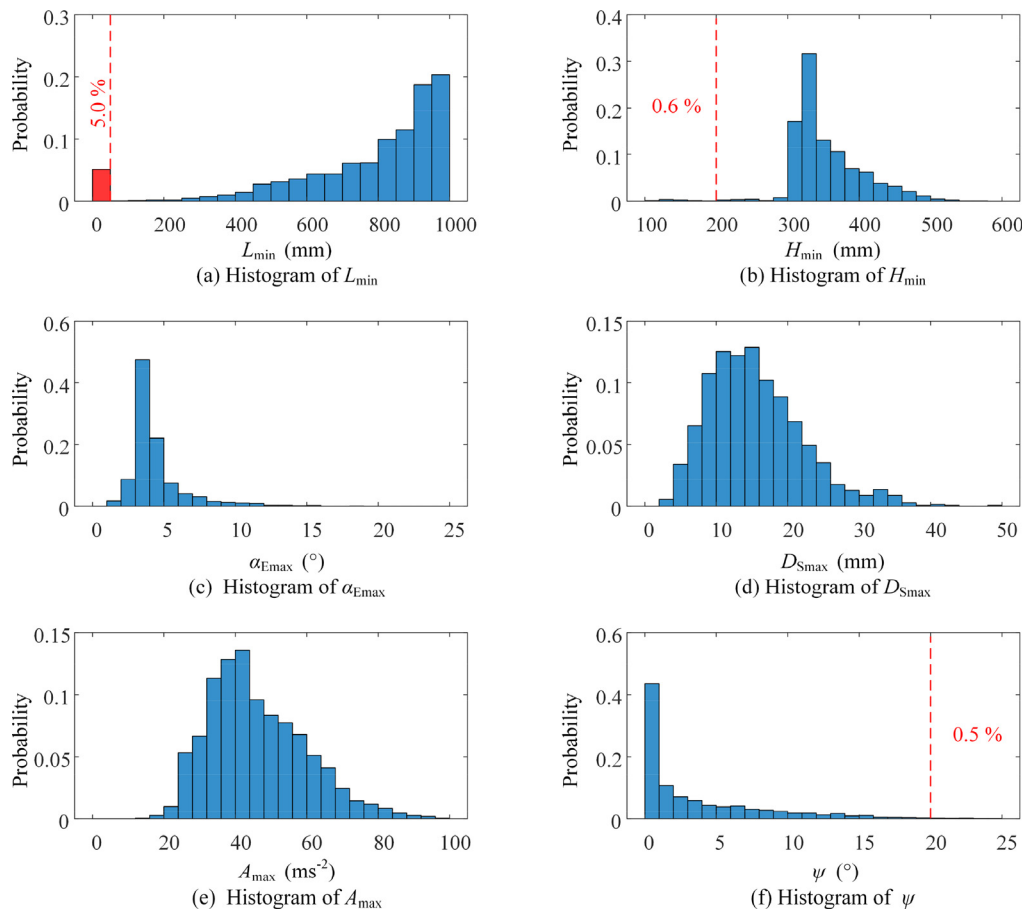
**Fig. 14** Histogram of Monte Carlo Simulation outputs.
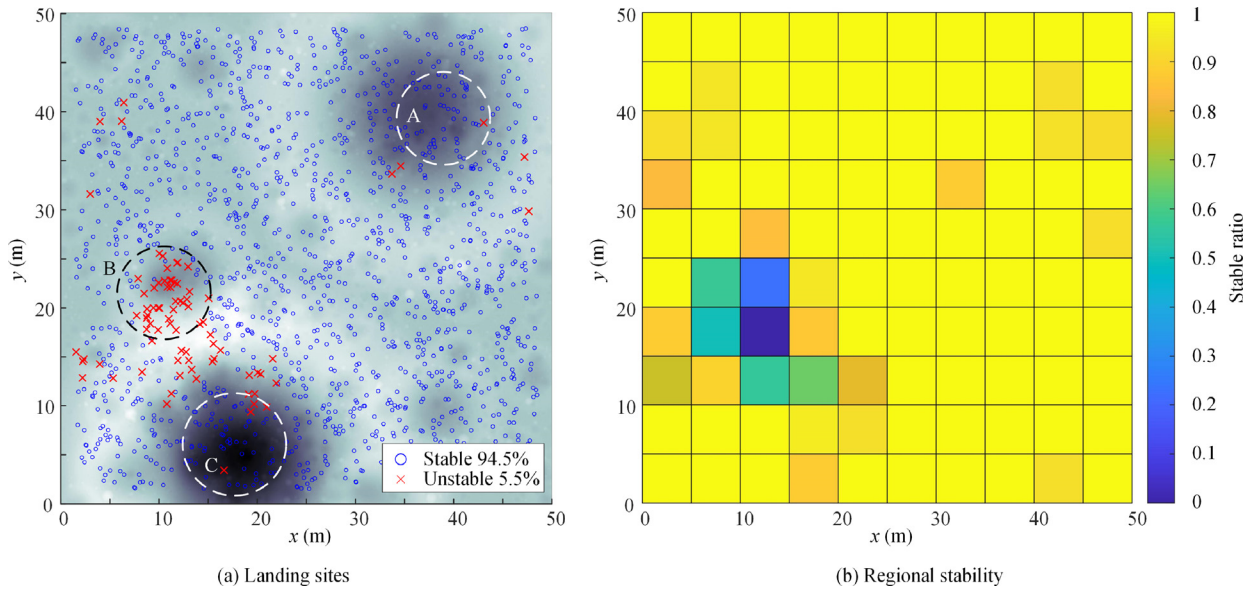


**Fig. 15** Landing sites on generated terrain and regional stability.

The simulation results are compared with the previous. As expected, when deactivating the attitude control thrusters, the overall stability is decreased with the overturning ratio increasing from 5.0% to 8.9%, as shown in Table 6. The stable ratio is 94.5% when the attitude control thrusters are used, and it decreases to 90.7% when thrusters are deactivated.

Concretely, the box plots, which contain the median, quartiles, extreme values, and outliers, are shown in Fig. 16. Most outputs are worse except for $H_{min}$ when the attitude control thrusters are closed. Take the median as an example: $L_{min}$ $L_{min}$ decreased from 852.2 mm to 838.9 mm, $\alpha_{Emax}$ $\alpha_{Emax}$ increased from 3.86° to 3.87°, $D_{Smax}$ $D_{Smax}$ increased from 14.6 mm to 14.8 mm, $A_{max}$ $A_{max}$ increased from 43.7 m/s² to 44.3 m/s², and $\psi$ increased from 1.50° to 1.63°. The variation trend of the quartile, the maximum value, and the minimum value are consistent with the median.

Overall, when the thrusters are used, the landing stability is improved by 3.8% in the whole 50 m × 50 m landing area. Referring to Eq.(3), when the landing surface is relatively flat, the thrust is usually low, and in this situation, the difference

**Table 6**   Stability when thrusters are on and off.

| Attitude control thrusters | On | Off |
|---|---|---|
| Overturning (%) | 5.0 | 8.9 |
| Other failure (%) | 0.5 | 0.4 |
| Stable (%) | 94.5 | 90.7 |
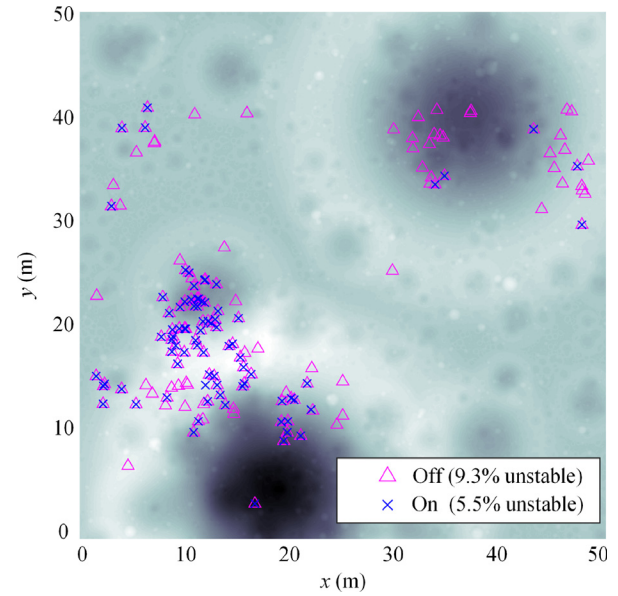


**Fig. 17**   Unstable landing sites when thrusters are on and off.
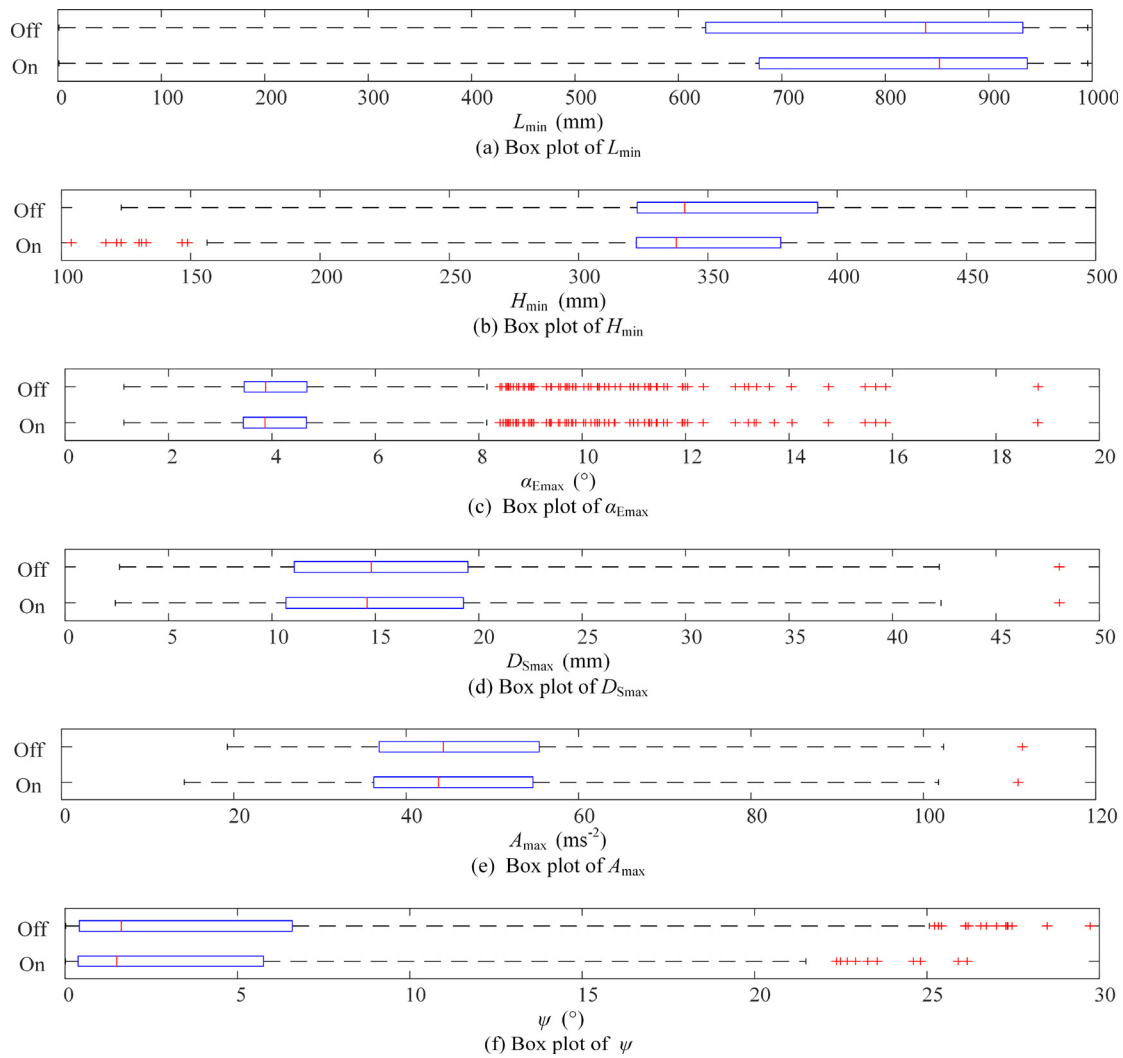


**Fig. 16**   Box plot of simulation outputs with and without control thrusters.

between landing with thrust on and off is slight. When the landing surface is rough, the moment provided by thrusters can significantly enhance the anti-overturning ability, even if the thrust action time is short. Fig. 17 shows the unstable landing sites when thrusters are on and off. In a bad local area around the crater, it can be observed that the unstable samples are significantly reduced when using thrusters. The comparison results validate the positive effects of attitude control thrusters.

## 7. Conclusions

(1) A multi-body dynamics modeling method for a Mars lander is developed in this paper. The pseudo-rigid body method is used to model the plastic deformation parts for fast computation. And the nonlinear spring-damping model and modified Coulomb friction model with correction terms are used to model the contact. In addition, 10 GNC attitude control thrusters are activated to improve the anti-overturning ability during landing.

(2) The effectiveness and accuracy of the dynamic modeling method are verified by experiments. The average error of secondary struts buffering strokes is 10%, and the average error of minimum distance between the origin and the landing terrain is 0.25%.

(3) A random landing terrain generation method based on statistical data is proposed. A 50 m × 50 m random terrain is obtained by linear superposition of randomly generated craters and rocks with regular shape. The establishment of random terrain benefits the analysis of the terrain adaptability of the Mars lander.

(4) 1500 sets of soft landing simulations are performed to analyze the landing stability and the effects of attitude control thrusters under uncertain terrain. The results show that the insecurity rate is 5.5%, in which the primary failure forms are overturning and abnormal posture caused by rough terrain. Another 1500 simulations without thrusters are performed. And the results suggest that the attitude thrusters can improve the landing performance under rough terrain.

## Declaration of Competing Interest

The authors declare that they have no known competing financial interests or personal relationships that could have appeared to influence the work reported in this paper.

## Acknowledgments

## References

1. Qian YQ, Xiao L, Zhao SY, et al. Geology and scientific significance of the rümker region in northern Oceanus procellarum: China's Chang'E-5 landing region. *J Geophys Res Planets* 2018;**123**(6):1407–30.
2. Wu Bo, Huang J, Li Y, et al. Rock abundance and crater density in the candidate Chang'E-5 landing region on the moon. *J Geophys Res Planets* 2018;**123**(12):3256–72.
3. Cohen BA, Chavers DG, Ballard BW. NASA'S robotic lunar lander development project. *Acta Astronaut* 2012;**79**:221–40.
4. Martín-Torres FJ, Zorzano M-P, Valentín-Serrano P, et al. Transient liquid water and water activity at Gale crater on Mars. *Nat Geosci* 2015;**8**(5):357–61.
5. Witze A. Touch down! NASA's Mars landing Sparks new era of exploration. *Nature* 2021;**590**(7847):535–7.
6. Wan WX, Wang C, Li CL, et al. China's first mission to Mars. *Nat Astron* 2020;**4**(7):721.
7. Rogers WF. Apollo experience report lunar module landing gear subsystem. Washington.D.C: NASA;1972. Report No.:TN D-6850.
8. Muraca CJ, King C. A Monte Carlo analysis of the Viking lander dynamics at touchdown. Washington.D.C: NASA;1975. Report No.:TN D-7959.
9. Han Y, Guo W, Gao F, et al. A new dimension design method for the cantilever-type legged lander based on truss-mechanism transformation. *Mech Mach Theory* 2019;**142**:103611.
10. Folkner WM, Dehant V, Le Maistre S, et al. The rotation and interior structure experiment on the InSight mission to Mars. *Space Sci Rev* 2018;**214**(5):100.
11. Li C, Liu J, Ren X, et al. The Chang'e 3 mission overview. *Space Sci Rev* 2015;**190**(1-4):85–101.
12. Maeda T, Ozaki T, Hara S, et al. Touchdown dynamics of planetary lander with translation-rotation motion conversion mechanism. *J Spacecr Rockets* 2017;**54**(4):973–80.
13. Chen JB, Nie H, Wan JL, et al. Investigation on landing impact dynamic and low-gravity experiments for deep space lander. *Sci China Phys Mech Astron* 2014;**57**(10):1987–97.
14. Witte L, Schroeder S, Kempe H, et al. Experimental investigations of the comet lander Philae touchdown dynamics. *J Spacecr Rockets* 2014;**51**(6):1885–94.
15. Cole TJ, Bassler J, Cooper S, et al. The challenges of designing a lightweight spacecraft structure for landing on the lunar surface. *Acta Astronaut* 2012;**71**:83–91.
16. Reddy JN. An introduction to the finite element method. *J Press Vessel Technol* 1989;**111**(3):348–9.
17. Zheng G, Nie H, Luo M, et al. Parametric design and analysis on the landing gear of a planet lander using the response surface method. *Acta Astronaut* 2018;**148**:225–34.
18. Ma L, Shao Z, Chen W, et al. Trajectory optimization for lunar soft landing with a Hamiltonian-based adaptive mesh refinement strategy. *Adv Eng Softw* 2016;**100**:266–76.
19. Liu YY, Song SG, Li M, et al. Landing stability analysis for lunar landers using computer simulation experiments. *Int J Adv Robotic Syst* 2017;**14**(6):172988141774844.
20. Maeda T, Otsuki M, Hashimoto T, et al. Attitude stabilization for lunar and planetary lander with variable damper. *J Guid Control Dyn* 2016;**39**(8):1790–804.
21. Zheng G, Nie H, Chen J, et al. Dynamic analysis of lunar lander during soft landing using explicit finite element method. *Acta Astronaut* 2018;**148**:69–81.
22. Yue S, Nie H, Zhang M, et al. Optimization and performance analysis of oleo-honeycomb damper used in vertical landing reusable launch vehicle. *J Aerosp Eng* 2018;**31**(2):04018002.
23. Ulamec S, Biele J, Blazquez A, et al. Rosetta lander - Philae: landing preparations. *Acta Astronaut* 2015;**107**:79–86.
24. Ulamec S, Fantinati C, Maibaum M, et al. Rosetta lander - landing and operations on comet 67P/churyumov-gerasimenko. *Acta Astronaut* 2016;**125**:80–91.
25. Ding ZM, Wang CJ, Wu HY, et al. Stability analysis of explorer in soft landing mode of engine shutdown at touchdown. *Journal of Beijing University of Aeronautics and Astronautics* 2018; 44(3):614-620[Chinese].
26. Wu HY, Wang CJ, Ding JZ, et al. Dynamics simulation analysis for novel lander based on two kinds of landing mode. *2017 9th International Conference on Measuring Technology and Mecha-*

tronics Automation (ICMTMA). January 14-15, 2017, Changsha, China. IEEE, 2017:8–12.

27. Morris AB, Goldstein DB, Varghese PL, Trafton LM. Lunar dust transport resulting from single- and four-engine plume impingement. AIAA J 2016;**54**(4):1339–49.

28. Dado MH. Variable parametric pseudo-rigid-body model for large-deflection beams with end loads. Int J Non Linear Mech 2001;**36**(7):1123–33.

29. Wang WJ, Bi SS, Zhang LG. Dynamic modeling of compliant mechanisms based on 2R pseudo-rigid-body model. Appl Mech Mater 2012;**163**:277–80.

30. Batterson S, Benson H, Gault D, et al. Lunar surface models. Washington.D.C: NASA;1969. Report No.:SP-8023.

31. Arora V, Singh SP, Kundra TK. Damped model updating using complex updating parameters. J Sound Vib 2009;**320**(1-2):438–51.

32. Imregun M, Visser WJ, Imregun M, et al. A review of model updating techniques. Shock Vibrat Digest 1991;**23**(1):9–20.

33. Bao N, Wang C. A Monte Carlo simulation based inverse propagation method for stochastic model updating. Mech Syst Signal Process 2015;**60-61**:928–44.

34. Yang JZ. Landing buffer mechanism of spacecraft. 1st ed. Beijing: China Astronautic Press; 2015. p. 20-60 [Chinese].

35. Proppe C, Pradlwarter HJ, Schuëller GI. Equivalent linearization and Monte Carlo simulation in stochastic dynamics. Probabilistic Eng Mech 2003;**18**(1):1–15.